HAL open science

Experimental Observation of Multifractality in Fibonacci Chains

Mattis Reisner, Yanel Tahmi, Frédéric Piéchon, Ulrich Kuhl, Fabrice Mortessagne

To cite this version:

Mattis Reisner, Yanel Tahmi, Frédéric Piéchon, Ulrich Kuhl, Fabrice Mortessagne. Experimental Observation of Multifractality in Fibonacci Chains. 2022. hal-03739590

HAL Id: hal-03739590

https://hal.science/hal-03739590v1

Preprint submitted on 27 Jul 2022

HAL is a multi-disciplinary open access archive for the deposit and dissemination of scientific research documents, whether they are published or not. The documents may come from teaching and research institutions in France or abroad, or from public or private research centers.

L'archive ouverte pluridisciplinaire **HAL**, est destinée au dépôt et à la diffusion de documents scientifiques de niveau recherche, publiés ou non, émanant des établissements d'enseignement et de recherche français ou étrangers, des laboratoires publics ou privés.

Experimental Observation of Multifractality in Fibonacci Chains

Mattis Reisner,[1] Yanel Tahmi,[1] Frédéric Piéchon,[2] Ulrich Kuhl,[1] and Fabrice Mortessagne[1,*]

[1] *Université Côte d'Azur, CNRS, Institut de Physique de Nice (INPHYNI), 06108 Nice, France, EU*
[2] *Laboratoire de Physique des Solides, Université Paris-Saclay, 91400 Orsay, France, EU*

(Dated: July 27, 2022)

The tight-binding model for a chain, where the hopping constants follow a Fibonacci sequence, predicts multifractality in the spectrum and wavefunctions. Experimentally, we realise this model by chains of small dielectric resonators with high refractive index ($\epsilon_r \approx 45$) of cylindrical form that exhibit evanescent coupling. We show that the fractality of the measured local density of state (LDOS) is best understood when the sites are rearranged according to the similarities in their local surrounding, i.e., their conumbers. This allows us to deduce simple recursive construction schemes for the LDOS for the two cases of dominant strong and weak coupling, despite our limited resolution due to non-zero resonance width and size constraints. We calculate the fractal dimensions of the wavefunctions and find good agreement with theoretical formulations for the multifractality based on a perturbative description in the quasi periodic limit.

The question of understanding wave propagation phenomena in inhomogeneous media transcends almost all types of waves (gravitational, seismic, sound, fluid, electromagnetic, and quantum), ranging from the largest to the smallest wavelength and frequency scales imaginable. Since the fundamental work of P. W. Anderson on quantum electrons in disordered systems[1], it is well established that interference effects induced by multiple random elastic scatterings can strongly modify wave propagation in such a way that, depending on the strength of the disorder, three regimes can be distinguished. For a "weak disorder", such that the mean free path of the scattering ℓ is much larger than the considered wavelength λ, the waves remain extended and propagate in a diffuse way. For a "strong disorder" ($\ell \ll \lambda$), the waves are "exponentially localized" in real space and cannot propagate anymore. At the transition between these two regimes, there is a critical regime characterized by a multifractal distribution of wave amplitudes in real space and associated with an anomalous diffusive propagation of wave packets [2–8]. Several recent experiments have succeeded in revealing such a critical regime with multifractal waves[9–12].

Beyond the disordered systems at the critical point, many numerical studies have shown that waves propagating in quasi-crystalline structures have generically multifractal properties with the particularity of having tunable fractal dimensions[13–17]. Several works have linked these fractal properties of waves to the specific geometrical properties of quasi-periodic lattices (2D tilings and 1D chains)[18–29]. Specifically, although quasicrystalline structures are not periodic, they exhibit long-range orientational and translational order and possess properties of self-similarity and high translational repeatability for domains of all scales. Nevertheless, nearly forty years after the discovery of quasicrystals [30], there is currently no experiment in real or meta materials that has clearly demonstrated these multifractal properties of waves, even in the simplest and most studied paradigmatic example that is the Fibonacci chain (see the recent review by A. Jagannathan[31]). However, a recent experiment using cavity polaritons propagating in a Fibonacci chain structure has succeeded in revealing the fractal character of the eigenfrequency spectrum and also in verifying the gap labeling in agreement with theoretical predictions[32].

In this work we present, on the one hand, the first experiment that explicitly demonstrates the existence of a simple recursive scheme to reconstruct the fractal properties of the local density of states of the waves on the Fibonacci chain. On the other hand, we quantitatively characterize these multifractal properties and show good agreement between the measured fractal dimensions and those predicted by the simplest modeling of the experiment.

For our experimental studies we use a versatile microwave setup that implements a tight-binding system[33]. It is based on high index cylindrical dielectric resonators (TiZrNbZnO, Exxelia serie E6000, $n \approx 6.7$, radius $r = 3\,\mathrm{mm}$, height $h = 5\,\mathrm{mm}$) sandwiched between two metallic plates and evanescently coupled. The isolated resonators have a resonance frequency at $\nu_0 \approx 7.45\,\mathrm{GHz}$ with a line width of $\Gamma \approx 2\,\mathrm{MHz}$. The variation of ν_0 for the resonators is within their width. For further details on the experimental setup and its relevance for topological photonics, see [34].

The experimental chains are built following the cut and project method (C&P). The C&P method can be used to construct all n-th periodic approximates C_n of the Fibonacci chain, up to its quasiperiodic structure for $n \to \infty$. It consists in projecting sites in a given interval of a 2D regular grid onto a line that is cutting the grid with a slope $\omega_n = F_{n-1}/F_{n-2}$, as can be be seen in Fig. 1(a). The F_n are the Fibonacci numbers defined via $F_n = F_{n-2} + F_{n-1}$ with $F_1 = 1$ and $F_2 = 1$. Note that in the limit $n \to \infty$, the slope ω_n tends toward the golden ratio $\omega = \omega_\infty = \frac{1+\sqrt{5}}{2}$. Due to the irrational nature of ω, the resulting structure is quasiperiodic, whereas for any rational approximation ω_n, the C_n chain exhibits an

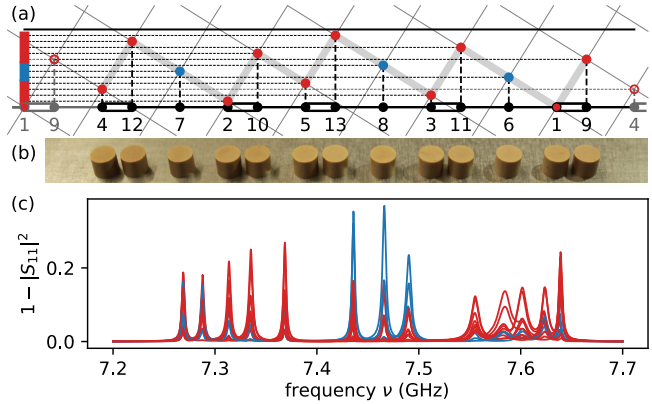

FIG. 1. (a) Example of the cut and project method for the 7-th approximate defined by a slope $\omega_7 = 8/5$ and a motif of $F_7 = 13$ sites. The projection on the horizontal axis dictates the arrangement of the sites of the chain according to strong (black double-line) and weak (black line) couplings. Each site is reordered according to its local environment on the perpendicular (vertical) axis, the resulting conumber $c(i)$ is indicated under each site at position i. Along the perpendicular axis, "atomic" (in blue) and "molecular" (in red) sites are clustered in 3 groups. (b) Photo of an experimental Fibonacci chain made of 13 resonators. (c) Measured reflection spectra $1-|S_{11}|^2$ for each resonator in the chain shown in (b, where the colors differentiate the atomic (blue) and molecular (red) sites.

infinite repetition of the same pattern of F_n sites.

The projected points (black points in Fig. 1(a)) divide the line in intervals that only have two different lengths A (black line) and B (black double-line). In a sequence of F_n intervals, the ratio between the number of A and B is given by ω_n. Very differently, the sites projected onto the perpendicular axis occupy equally spaced and reordered positions: The sites whose projection on the horizontal axis are surrounded by two A intervals (further referred as atomic sites) are clustered around the center, whereas those embedded in ABA sequences (further referred as molecular sites) are grouped at the sides – at the bottom for the sites between AB, at the top for BA. This way of referring to the sites not by their index i but by their projection on the perpendicular axis [see Fig. 1(a)] is called conumbering and was first introduced by R. Mosseri[35, 36].

From there, different experimental strategies can be followed: either the two letters are associated to two different couplings between resonators, or they are used to account for two different resonant frequencies. We will implement the first one here, thus introducing two coupling, t_A and t_B, or, equivalently, two distances d_A and d_B. This experimental choice offers two scenarios: either $\rho = t_A/t_B > 1$, that corresponds to the dominant strong coupling scenario, or $\rho = t_A/t_B < 1$, the dominant weak coupling scenario. The main part of the study reported here will make the use of the second scenario, but we will show at the end that inverting ρ yields interesting results too. Fig. 1(b) shows the experimental realization of a chain of 13 resonators using the direct pattern created by the C&P procedure. In this case, the dominant weak coupling regime is implemented. For an experimental reason explained below, the last weak coupling is suppressed. This procedure has also the advantage that the experimental chain reproducing an elementary motif of a C_n Fibonacci-approximate generates F_n collective resonance peaks, as can be seen in the spectra plotted on Fig. 1(c), where each spectrum is measured individually by a movable loop antenna placed directly over each resonator[33]. This correspondence between the number of resonators and resonances was expected from the fact that the experiment enters into the scope of a tight-binding model with nearest-neighbor couplings[33].

The spectra measured at molecular site positions are plotted in red, and in blue for atomic sites. It is worth noting that the bunching of sites reveals by the conumbering procedure has its counterpart in the spectrum. Indeed, one can clearly see that the three resonances within the central band are mainly localized on atomic sites, while the two side bands are dominated by states located at the molecular sites. This correspondence of the frequency index of states and the conumber index of sites arises from the equivalent paths of renormalization that are used to describe band-labels and sites in a perturbative renormalization scheme, when the chains are constructed by a recursive inflation [28, 37].

In a first step, the experimental Fibonacci chains we implement are limited to a single repetition of a F_n-letter motif, with an averaging over different allowed permutations. In order to reduce finite-size effects, we constrain the experiment to permutations that *(i)* generate patterns whose infinite repetitions C_n would be linked by weak coupling, and *(ii)* impose that the elementary chain ends on both sides by a strong coupling. Each chain is thus made of F_n sites and $F_n - 1$ couplings, as illustrated in Fig. 1(b) for $F_7 = 13$. In practice, for a motif of $F_{10} = 55$ resonators, in the dominant weak coupling regime ($\rho < 1$), there are 8 different permutations that start and end on a strong coupling.

We measure the spectrum over each resonator for all permutations for the coupling strengths $t_A = 81\,\mathrm{MHz}$ and $t_B = 126\,\mathrm{MHz}$, corresponding to distances $d_A = 8\,\mathrm{mm}$ and $d_B = 7\,\mathrm{mm}$. The relation between coupling strength t and separation d between two resonators is extracted from two-resonator measurements [33, 34]. We chose these values in order to have the least possible overlap between resonances in the spectra, while keeping ρ reasonably small, for the best visible contrast. The resonance amplitudes $\psi_j(i)$ of each peak j of the measured spectrum above resonator i are extracted via a harmonic inversion method [38, 39] and a density-based clustering algorithm [40]. Additionally, we symmetrize the results

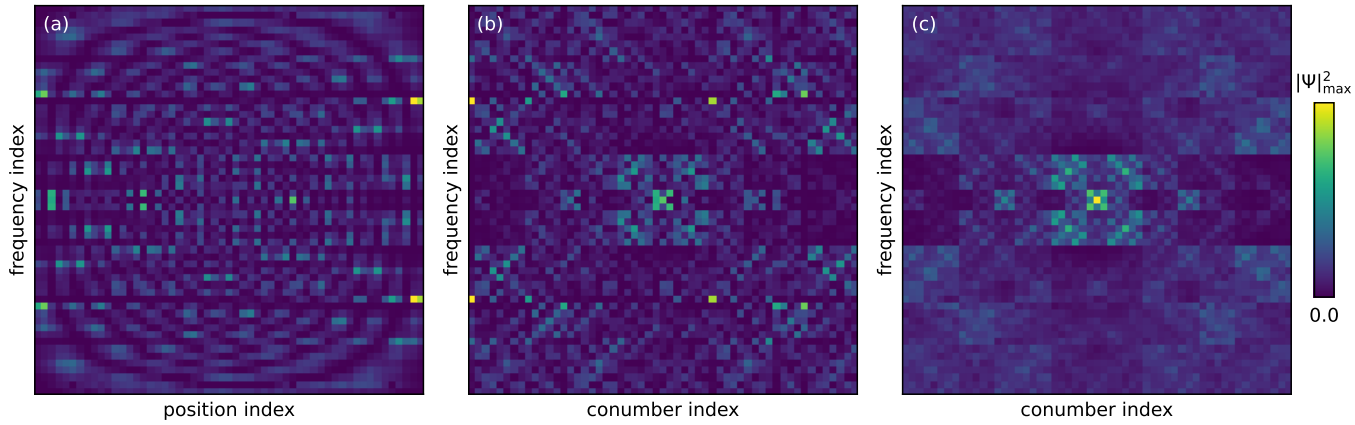

FIG. 2. Experimentally extracted LDoS of a single configuration of 55 resonators arranged according to their position index i (a), rearranged according to the conumber index $c(i)$ (b) and the average over all 8 permutations (c).

with respect to the central frequency-index as the resonance widths for the higher frequency bands are larger and thus stronger overlapping making it impossible to extract [34]. Finally we obtain a discretized form of the local density of states $\mathrm{LDoS}(i,j) = |\psi_j(i)|^2$, where $|\psi_j(i)|^2$ represents the wavefunction intensity of state j evaluated over resonator i [33, 34]. An example spectrum, a detailed description of the data analysis and the LDoS for all configurations can be found in the Supplemental Material [41].

In Fig. 2(a) we present the resulting $\mathrm{LDoS}(i,j)$ for each position index i of the 55 resonators for a single configuration. Fig. 2(b) shows a rearranging of the LDoS according to their conumber: $\mathrm{LDoS}(c(i),j)$, and (c) the average over the 8 permutations. In Fig. 2(a), LDoS exhibit typical standing-wave interference patterns due to the finite-size of the chain[42], but no hierarchical structure is visible. Reordering the LDoS based on the conumber index provides insight into fractal structures, that are completely revealed by the average over all permutations [see Fig. 2(c)]. The symmetry between frequency index j and conumber index $c(i)$ is clearly visible: The plot is almost invariant under the exchange of the conumber/frequency axis.

In order to give a more quantitative characterization of the fractality, and especially the multifractal aspect of the wavefunctions, we investigate the fractal dimensions $D_q^\psi(j)$ of the wavefunctions [28], that are defined via an exponential scaling of the generalized inverse participation number with the motif length F_n as follows

$$\chi_q^{(n)}(j) = \sum_i |\psi_j^{(n)}(i)|^{2q} \underset{n\to\infty}{\sim} F_n^{-(q-1)D_q^\psi(j)} . \quad (1)$$

For systems that exhibit multifractal wavefunctions like quasicrystal or disordered systems at criticality, the fractal dimensions $D_q^\psi(j)$ decrease when q increases. This property is related to the fact that the region with high wave function probability are rarer [6, 7].

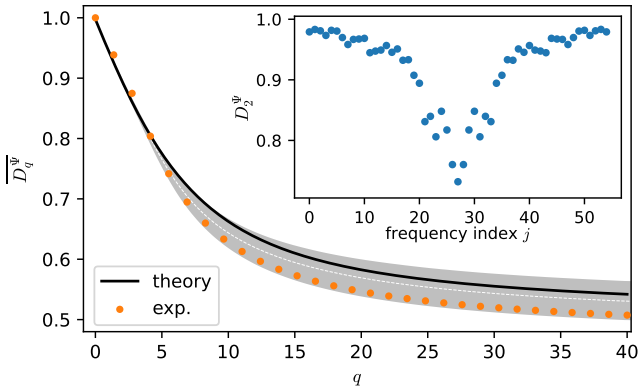

FIG. 3. Frequency averaged fractal dimension $\overline{D_q^\psi}$ versus the multifractal parameter q, experimentally extracted using a box-counting method (orange points) compared to theoretical predictions (solid black line). The grey area highlights the 90 % confidence interval obtained from tight-binding simulations (see Supplemental Material [41]), the dashed line indicates the mean expectation value. The inset shows $D_2^\psi(j)$ for all states j.

One can further define the frequency-averaged fractal dimension of wavefunctions $\overline{D_q^\psi}$ by averaging over all states [28]

$$\left\langle \chi_q^n(j) \right\rangle_j = \frac{1}{F_n} \sum_j \chi_q^{(n)}(j) \underset{n\to\infty}{\sim} F_n^{-(q-1)\overline{D_q^\psi}} . \quad (2)$$

As $F_{10} = 55$ is far from the limit $n \to \infty$, we extract the multifractal dimensions using a box-counting algorithm on the LDoS of Fig. 2(c) [43]. For a detailed description of the procedure see Supplemental Material [41].

In Fig. 3 one can see the extracted frequency-averaged fractal dimension $\overline{D_q^\psi}$ as a function of the multifractal parameter q (orange points). The inset shows the fractal dimensions, $D_2^\psi(j)$ for all states j, which is equivalent to

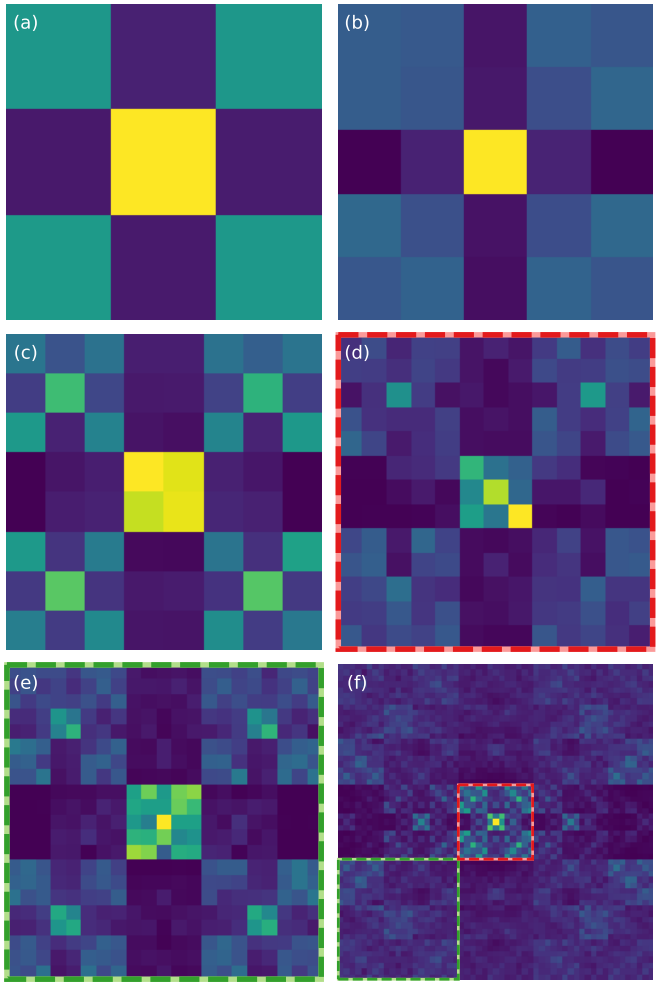

FIG. 4. Conumber-averaged LDoS for different motif length F_n: (a) $F_4 = 3$, (b) $F_5 = 5$, (c) $F_6 = 8$, (d) $F_7 = 13$, (e) $F_8 = 21$ and (f) $F_n = 55$ (already presented in Fig. 2). For all plots the horizontal axis corresponds to the conumber index $c(i)$ and the vertical axis to the frequency index j, and the same colormap as in Fig. 2 is used. The green and red squares highlight the recursive construction.

the inverse participation ratio. There are large fluctuations with respect to the mean value with a very distinct dip for the central state. Thus, the central state is the most localized and has the lowest fractal dimensions, while the highest/lowest states are the most extended ones.

We compare the frequency-averaged fractal dimension $\overline{D_q^\psi}$ obtained experimentally with a theoretical prediction based on a renormalization group approach, formulated in the limit $\rho \ll 1$ and developed until the order ρ^{4q} [28]; in the experiment $\rho = 0.64$. We further estimate a 90 % confidence interval for the experiment, by performing tight-binding simulations of the system that account for the variances in the positioning of the resonators and the fluctuations of their resonance frequency. Details on the procedure can be found in the Supplemental Material [41]. Although far from the strong modulation limit ($\rho \ll 1$), a good agreement between experimental and theoretical values of $\overline{D_q^\psi}$ is obtained, both curves lie within the estimated confidence interval (see Fig. 3). For large q, an offset is noticeable between theory and experiment, that could eventually be explained by experimental fluctuations, but even the average value of the simulated $\overline{D_q^\psi}$ (white dashed line) shows an offset. This is mainly due to the finite system size, since the theory was formulated in the quasiperiodic limit (see Supplemental Material [41]). Note that, although equation (2) is invariant to inverting index $c(i)$ and j, our method to calculate $\overline{D_q^\psi}$ via a box counting algorithm is not. Nevertheless, interchanging the conumbering index $c(i)$ with the frequency index j upon the calculation of $\overline{D_q^\psi}$ leads to two hardly distinguishable curves (not shown in Fig. 3), further emphasizing the equivalence between conumbers and frequencies.

Another aspect often refereed to fractality is the self similarity of structures [18, 19, 21–23, 27, 29]. Similar to the recursive construction of the Fibonacci numbers F_n, the complete LDoS can be constructed recursively. The procedure is based on the renormalization of atomic and molecular sites [28]

$$|\psi_j^{(n)}(c_i)|^2 = \overline{\lambda} \cdot |\psi_{j'}^{(n-3)}(c_{i'})|^2 \quad \text{if } j \text{ is atomic,} \tag{3}$$

$$|\psi_j^{(n)}(c_i)|^2 = \lambda \cdot |\psi_{j'}^{(n-2)}(c_{i'})|^2 \quad \text{if } j \text{ is molecular,} \tag{4}$$

where $\overline{\lambda}$ and λ are renormalization factors that depend on ρ.

We investigate this recursive construction by experimentally realizing the first periodic approximates (i.e. $F_n = 3, 5, 8, 13, 21$). Instead of using different permutations of the periodic motif, as we have done previously, we use circular chains, where the basic motif with F_n sites is repeated N_p times. The number of repetitions N_p is chosen such that a ring of around 100 resonators is build for each F_n-motif. In this way the F_n bands, expected for an infinite chain C_n, are each populated with N_p states, in contrast to the previous experiment, where a single state was defining the band position. Due to the higher density of states inside the bands an individual extraction of resonance is not possible anymore and we extracted the LDoS directly from the reflection spectra, where we reduced the weaker coupling to $t_A = 55\,\text{MHz}$, and enhance the stronger to $t_B = 148\,\text{MHz}$, in order to obtain better isolated bands (for details see Supplemental Material [41]). This allows us to average over equivalent sites and states.

In Fig. 4 we present the LDoS for the first approximates. Especially highlighted for $F_{10} = 55, F_8 = 21$ and $F_7 = 13$ (Fig. 4(f), (e) and (d), respectively], the central square (marked in red), which gathers atomic sites and their corresponding states, of the LDoS at order n resembles at the complete LDoS of order $n - 3$, and the

four squares in the corners (molecular sites and frequencies, one marked in green) of the LDoS at order n resemble at the complete LDoS of order $n-2$. The recursive construction is also well visible for smaller n. We calculate the renormalization factor $\overline{\lambda}$ by integrating the central square (corresponding to atomic sites and states) and λ by integrating and averaging over the four corner squares (corresponding to molecular sites and states) in Fig. 4(f). We find $\overline{\lambda} = 0.51$ and $\lambda = 0.42$, which are in reasonable good agreement with theoretical predictions for the quasiperiodic limit $\overline{\lambda}_{\text{theo}} = 0.48$ and $\lambda_{\text{theo}} = 0.43$ for $\rho = 0.64$. Further information about the theoretical predictions and the experimental estimation of the renormalization factors can be found in the Supplemental Material [41].

As already mentioned before, although we mainly focus our quantitative analyses on the common case of $\rho < 1$, we also experimentally investigate the system with interchanged couplings: t_B is now the weaker coupling and t_A the stronger, $\rho > 1$, thus the strong coupling dominates. As for the system with $\rho < 1$ we investigate the large system ($F_n = 55$) by averaging over the 21 different permutations that meet the constraints, and smaller systems by means of circular chains. The extracted LDoS can be seen in Fig. 5. Instead of single atoms and dimers, as for $\rho < 1$, the chains are now composed by dimers and trimers. This results in a different renormalization scheme upon the first deflation of the chain. The effective bond couplings between two neighboring trimers take on only two possible values, arranged according to a Fibonacci sequence but with inverted strong and weak couplings. One thus passes from the chain C_n to the chain C_{n-3} with $\rho \to 1/\rho$ when appropriately renormalizing their couplings. In the same way one passes from the chain C_n to the chain C_{n-4} again with $\rho \to 1/\rho$ for the dimers. All further deflation steps then follow the renormalization laws for $\rho < 1$ [24]. This explains why the general structure in Fig. 5 is quite different, but we find the same basic motifs as in Fig. 4. The red square in Fig. 5(b) highlights the basic motif associated with the trimers, that can be found in Fig. 4(d,f), while the orange square highlights the basic motif associated with the dimers, which again can be found in Fig. 4(c).

In this Letter, we have shown that the multifractal properties of waves propagating on a quasiperiodic lattice can be unambiguously observed in our finite-size experimental set-up made of coupled dielectric resonators. Our measurements were successfully analyzed using a renormalization group approach. The robustness of the fractality observed will be challenged in the near future by introducing controlled disorders in the experiment [44]. Either a coupling disorder, induced by small variation of distances between microwave resonators, or a phason disorder, resulting from a local inversion of short and strong bond and giving birth to configuration that cannot be obtained by permutation. Our microwave experimental platform is also well suited to the study of 2D lattices [34], and has been already used to provide new physical insights on the behavior of waves on a Penrose tiling [45]. Due to the physical couplings that are not constrained to the edges of the tiles, the tight-binding model implemented in the lattice is not the one usually theoretically and numerically studied. Thus by implementing 2D tiling of codimension 1 [35] in our experiment, as for example the Rauzy tiling [46], one can expect to exhibit richer multifractal properties.

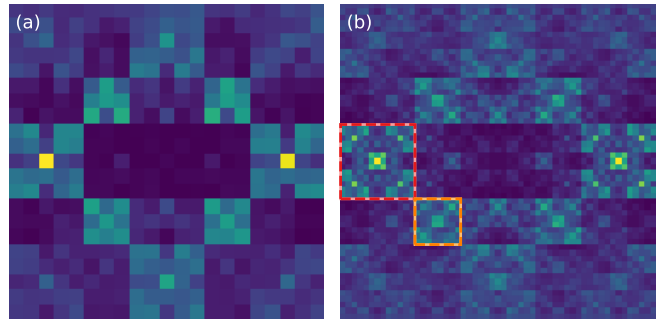

FIG. 5. LDoS for motif length $F_8 = 21$ (a) and $F_{10} = 55$ (b) for $\rho < 1$. The x-axis corresponds to the conumber index $c(i)$ and the y-axis to the frequency index j and the same colormap as in Fig. 2 is used. The red and orange square highlight the basic motifs.

* fabrice.mortessagne@univ-cotedazur.fr

[1] P. W. Anderson, Absence of diffusion in certain random lattices, Phys. Rev. **109**, 1492 (1958).
[2] F. Wegner, Inverse participation ratio in 2+ϵ dimensions, Zeitschrift für Physik B Condensed Matter **36**, 209 (1980).
[3] M. Schreiber and H. Grussbach, Multifractal wave functions at the Anderson transition, Phys. Rev. Lett. **67**, 607 (1991).
[4] U. Fastenrath, M. Janßen, and W. Pook, Multifractal analysis of disorder induced metal-insulator transitions, Physica A: Statistical Mechanics and its Applications **191**, 401 (1992).
[5] M. Schreiber, Multifractal characteristics of electronic wave functions in disordered systems, in *Computational Physics: Selected Methods Simple Exercises Serious Applications*, edited by K. H. Hoffmann and M. Schreiber (Springer Berlin Heidelberg, Berlin, Heidelberg, 1996) pp. 147–165.
[6] T. Brandes, B. Huckestein, and L. Schweitzer, Critical dynamics and multifractal exponents at the Anderson transition in 3d disordered systems, Annalen der Physik **508**, 633 (1996).
[7] B. Huckestein and R. Klesse, Spatial and spectral multifractality of the local density of states at the mobility edge, Phys. Rev. B **55**, R7303 (1997).
[8] F. Evers and A. D. Mirlin, Anderson transitions, Rev. Mod. Phys. **80**, 1355 (2008).

[9] M. Morgenstern, J. Klijn, C. Meyer, and R. Wiesendanger, Real-space observation of drift states in a two-dimensional electron system at high magnetic fields, Phys. Rev. Lett. **90**, 056804 (2003).

[10] K. Hashimoto, C. Sohrmann, J. Wiebe, T. Inaoka, F. Meier, Y. Hirayama, R. A. Römer, R. Wiesendanger, and M. Morgenstern, Quantum Hall transition in real space: From localized to extended states, Phys. Rev. Lett. **101**, 256802 (2008).

[11] S. Faez, A. Strybulevych, J. H. Page, A. Lagendijk, and B. A. van Tiggelen, Observation of multifractality in Anderson localization of ultrasound, Phys. Rev. Lett. **103**, 155703 (2009).

[12] B. Jäck, F. Zinser, E. J. König, S. N. P. Wissing, A. B. Schmidt, M. Donath, K. Kern, and C. R. Ast, Visualizing the multifractal wave functions of a disordered two-dimensional electron gas, Phys. Rev. Research **3**, 013022 (2021).

[13] M. Kohmoto, L. P. Kadanoff, and C. Tang, Localization problem in one dimension: Mapping and escape, Phys. Rev. Lett. **50**, 1870 (1983).

[14] T. Fujiwara, M. Arai, T. Tokihiro, and M. Kohmoto, Localized states and self-similar states of electrons on a two-dimensional Penrose lattice, Phys. Rev. B **37**, 2797 (1988).

[15] T. Fujiwara, M. Kohmoto, and T. Tokihiro, Multifractal wave functions on a Fibonacci lattice, Phys. Rev. B **40**, 7413 (1989).

[16] A. Chhabra and R. V. Jensen, Direct determination of the f(α) singularity spectrum, Phys. Rev. Lett. **62**, 1327 (1989).

[17] H. Tsunetsugu, T. Fujiwara, K. Ueda, and T. Tokihiro, Electronic properties of the Penrose lattice. I. Energy spectrum and wave functions, Phys. Rev. B **43**, 8879 (1991).

[18] M. Kohmoto and B. Sutherland, Electronic states on a Penrose lattice, Phys. Rev. Lett. **56**, 2740 (1986).

[19] B. Sutherland, Self-similar ground-state wave function for electrons on a two-dimensional Penrose lattice, Phys. Rev. B **34**, 3904 (1986).

[20] Q. Niu and F. Nori, Renormalization-group study of one-dimensional quasiperiodic systems, Phys. Rev. Lett. **57**, 2057 (1986).

[21] M. Kohmoto, B. Sutherland, and C. Tang, Critical wave functions and a Cantor-set spectrum of a one-dimensional quasicrystal model, Phys. Rev. B **35**, 1020 (1987).

[22] B. Sutherland, Critical electronic wave functions on quasiperiodic lattices: Exact calculation of fractal measures, Phys. Rev. B **35**, 9529 (1987).

[23] T. Tokihiro, T. Fujiwara, and M. Arai, Exact eigenstates on a two-dimensional Penrose lattice and their fractal dimensions, Phys. Rev. B **38**, 5981 (1988).

[24] Q. Niu and F. Nori, Spectral splitting and wave-function scaling in quasicrystalline and hierarchical structures, Phys. Rev. B **42**, 10329 (1990).

[25] M. Holzer, Multifractal wave functions on a class of one-dimensional quasicrystals: Exact f(α) curves and the limit of dilute quasiperiodic impurities, Phys. Rev. B **44**, 2085 (1991).

[26] F. Piéchon, Anomalous diffusion properties of wave packets on quasiperiodic chains, Phys. Rev. Lett. **76**, 4372 (1996).

[27] P. Repetowicz, U. Grimm, and M. Schreiber, Exact eigenstates of tight-binding Hamiltonians on the Penrose tiling, Phys. Rev. B **58**, 13482 (1998).

[28] N. Macé, A. Jagannathan, and F. Piéchon, Fractal dimensions of wave functions and local spectral measures on the Fibonacci chain, Phys. Rev. B **93**, 205153 (2016).

[29] N. Macé, A. Jagannathan, P. Kalugin, R. Mosseri, and F. Piéchon, Critical eigenstates and their properties in one- and two-dimensional quasicrystals, Phys. Rev. B **96**, 045138 (2017).

[30] D. Shechtman, I. Blech, D. Gratias, and J. W. Cahn, Metallic phase with long-range orientational order and no translational symmetry, Phys. Rev. Lett. **53**, 1951 (1984).

[31] A. Jagannathan, The Fibonacci quasicrystal: Case study of hidden dimensions and multifractality, Rev. Mod. Phys. **93**, 045001 (2021).

[32] D. Tanese, E. Gurevich, F. Baboux, T. Jacqmin, A. Lemaître, E. Galopin, I. Sagnes, A. Amo, J. Bloch, and E. Akkermans, Fractal energy spectrum of a polariton gas in a Fibonacci quasiperiodic potential, Phys. Rev. Lett. **112**, 146404 (2014).

[33] M. Bellec, U. Kuhl, G. Montambaux, and F. Mortessagne, Tight-binding couplings in microwave artificial graphene, Phys. Rev. B **88**, 115437 (2013).

[34] M. Reisner, M. Bellec, U. Kuhl, and F. Mortessagne, Microwave resonator lattices for topological photonics [invited], Opt. Mater. Express **11**, 629 (2021).

[35] Sire, Clément and Mosseri, Rémy, Excitation spectrum, extended states, gap closing : some exact results for codimension one quasicrystals, J. Phys. France **51**, 1569 (1990).

[36] R. Mosseri, Contribution to the theory of quasicrystal approximants, in *Universalities in Condensed Matter*, edited by R. Jullien, L. Peliti, R. Rammal, and N. Boccara (Springer Berlin Heidelberg, Berlin, Heidelberg, 1988) pp. 9–14.

[37] S. Thiem and M. Schreiber, Renormalization group approach for the wave packet dynamics in golden-mean and silver-mean labyrinth tilings, Phys. Rev. B **85**, 224205 (2012).

[38] J. Main, Use of harmonic inversion techniques in semiclassical quantization and analysis of quantum spectra, Physics Reports **316**, 233 (1999).

[39] U. Kuhl, R. Höhmann, J. Main, and H.-J. Stöckmann, Resonance widths in open microwave cavities studied by harmonic inversion, Phys. Rev. Lett. **100**, 254101 (2008).

[40] G. J. Aubry, L. S. Froufe-Pérez, U. Kuhl, O. Legrand, F. Scheffold, and F. Mortessagne, Experimental tuning of transport regimes in hyperuniform disordered photonic materials, Phys. Rev. Lett. **125**, 127402 (2020).

[41] See Supplemental Material at [URL will be inserted by publisher] for more details and technical information on the data acquisition and analysis and the calculations of the fractal dimensions and renormalization factors. It includes the additional reference [47].

[42] C. Dutreix, M. Bellec, P. Delplace, and F. Mortessagne, Wavefront dislocations reveal the topology of quasi-1d photonic insulators, Nature Communications **12**, 3571 (2021).

[43] S. Thiem and M. Schreiber, Wavefunctions, quantum diffusion, and scaling exponents in golden-mean quasiperiodic tilings, Journal of Physics: Condensed Matter **25**, 075503 (2013).

[44] A. Moustaj, S. Kempkes, and C. M. Smith, Effects of disorder in the fibonacci quasicrystal, Phys. Rev. B **104**, 144201 (2021).

[45] P. Vignolo, M. Bellec, J. Böhm, A. Camara, J.-M. Gambaudo, U. Kuhl, and F. Mortessagne, Energy landscape in a Penrose tiling, Phys. Rev. B **93**, 075141 (2016).

[46] J. Vidal and R. Mosseri, Generalized Rauzy tilings: construction and electronic properties, Materials Science and Engineering: A **294-296**, 572 (2000).

[47] A. Rehemanjiang, M. Richter, U. Kuhl, and H.-J. Stöckmann, Microwave realization of the chiral orthogonal, unitary, and symplectic ensembles, Phys. Rev. Lett. **124**, 116801 (2020).

Supplemental Material for manuscript: Experimental Observation of Multifractality in Fibonacci Chains

by Mattis Reisner[1], Yanel Tahmi[1], Federic Piechon[1], Ulrich Kuhl[1], and Fabrice Mortessagne[1]
[1] Université Côte d'Azur, CNRS, Institut de Physique de Nice (INPHYNI), 06108 Nice, France, EU
[2] Laboratoire de Physique des Solides, Universitée Paris-Saclay, 91400 Orsay, France, EU

Extracting the local density of states from the measured spectra

A general presentation of our versatile tight-binding microwave experiment can be found in [33, 34]. In the following chapter we briefly point our the link between the measured reflection spectrum, local density of states and the eigenvectors of the tight-binding-system. We consider a tight-binding Hamiltonian $\mathcal{H}_{TB}$ that describes a system of N coupled resonators, with associated eigenvalues $\{\nu_j\}$ and eigenvectors $\{c^j\}$ that are used to describe the wavefunctions $\psi_j(\vec{r}) = \sum_i^N c_i^j \cdot \psi_0(\vec{r}-\vec{r_i}) = \sum_i^N \psi_n(i)$ of the tight-binding system, where $\psi_0(\vec{r})$ is the single resonator wavefunction and $\vec{r_i}$ the position of the resonators. Assuming a Breit-Wigner form of the scattering matrix and a constant antenna coupling σ throughout the whole frequency range, the reflection spectrum is then given by

$$S(\vec{r},\nu) = 1 - \mathrm{i}\sigma \sum_j^N \frac{|\psi_j(\vec{r})|^2}{\nu - \nu_j + \mathrm{i}\Gamma_j}, \tag{S1}$$

where Γ_j is the decay rate associated with state j and $\vec{r}$ is the position of the measuring antenna. One can then derive the local density of states

$$\rho(\vec{r},\nu) = \frac{1}{\pi\sigma}[1-\Re S(\vec{r},\nu)] = \sum_j |\Psi_j(\vec{r})|^2 \cdot f_{\nu_j,\Gamma_j}(\nu), \tag{S2}$$

where $f_{\nu_j,\Gamma_j}(\nu)$ are normalized Cauchy distributions around ν_j with width Γ_j ($\int_{-\infty}^{+\infty} f_{\nu_j,\Gamma_j}(\nu)d\nu = 1$). Due to the typical linewidths Γ of a few MHz, in our case of large N the resonance peaks in the spectrum, and thus in the density of states, are strongly overlapping. We therefore define a discretized version of the local density of states in the frequency as well in the space domain

$$\mathrm{LDoS}(i,j) = |\Psi_j(i)|^2 = |\Psi_j(\vec{r_i})|^2 = \lim_{\{\Gamma_j\}\to 0} \rho(\vec{r_i},\nu_j). \tag{S3}$$

This quantity is evaluated from the reflection spectra, by extracting all resonance amplitudes measured exactly over the center of each resonator. The resonance-amplitudes are normalized so that $\sum |\psi_j(i)|^2 = 1$ and they can be directly associated with the squared eigenvectors $|c_i^j|^2$ of the tight-binding Hamiltonian $\mathcal{H}_{TB}$.

For small system sizes ($N \lesssim 10$), direct fits of the spectra with a sum of complex Lorentz lines can be implemented[34]. For larger systems, the overlap between resonances becomes too strong, making the fitting strategy impractical. To extract the LDoS(i,j), we thus developed two different techniques depending weather we work with the linear chains of 55 resonators or the circular chains of around 100 resonators.

Harmonic Inversion and clustering algorithm

The linear chains are constituted of 55 resonators. A picture of one configuration, with dominant weak coupling can be seen in figure S1 (a). The resonators are numerated, in order to identify them and choose only resonators whose resonance frequencies are very close to each other. For the 55 resonators that we use, the difference between the highest and lowest frequencies is around 3 MHz, the same order of the single resonator linewidth Γ_0. The spectrum measured above the center of the resonator at position $i = 33$ of the chain can be seen in figure S1 (b), where one can clearly see the overlapping between resonance peaks.

In order to extract all resonance-amplitudes for each configuration we use a method based on an algorithm called Harmonic Inversion [39]. It is based on the fact that in the time-domain a complex Lorentz-line gives rise to an exponential function. Supposing that the time-signal (discrete signal with 2N points) only consists of N exponential functions with different complex amplitude and exponents, one can establish a set of non-linear equations in order to determine all of their parameters. Since the harmonic inversion tries to describe the whole spectrum with a sum of Lorentzian, we first have to filter out resonances induced by the non flat baseline of the reflection measurements and by the small fluctuations due to noise. An efficient filtering is obtained by keeping only the resonances whose widths and amplitudes are within a given interval. We then perform a clustering in order to follow each resonance from one antenna-position to the other, regrouping them and associate them with a certain state [40]. For each configuration we adjust the parameters of the density based clustering algorithm, so that we use the same parameters for all antenna-positions, to avoid to manually cluster/adjust states according to our expectations.

Figure S1 shows the partial reconstruction of the spec-

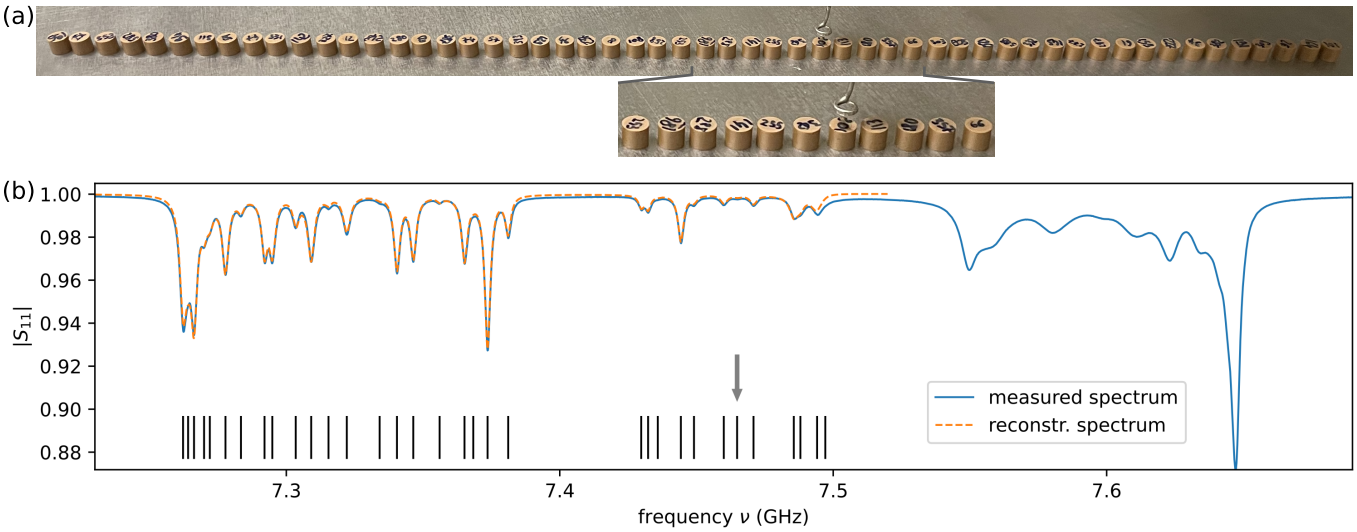

FIG. S1. (a) picture of the experimental chain of one permutation for the case of dominant weak coupling ($\rho = t_A/t_B < 1$). The metallic topplate that is normally placed above the resonators in order to reduce the system to two dimensions was removed in order to take the picture. Above the resonator at position 33 (counted from the left) we position the loop antenna trough which we measure the reflection spectra above each resonator. (b) reflection spectrum measured at position 33 and the reconstructed spectrum using the resonances obtained via the harmonic inversion method. The black vertical lines mark the extracted resonance positions and the grey arrow marks the central state ($j = 28$), above which we symetrize the LDoS(i, j) in order to span the whole frequency range. conf 6, index 32 (starting from 0), so 33th resonator

trum using the harmonic inversion algorithm, the black horizontal lines indicating the frequencies of the extracted resonances. The quality of the fit is excellent. We limit the reconstructed spectrum to the lower and central frequency band only, since, as described in [34], the higher frequency states have generally greater resonance-widths due to different effective antenna-couplings and larger ohmic losses. If only next-nearest-neighbour couplings are present, the system has a CT-symmetry [47] imposing that the spectrum is symmetric around the eigenfrequency of a single resonator. In our experiment we have a next-nearest-neighbour coupling of the order of only 5 % of the nearest-neighbour coupling. By consequences, the latter symmetry is almost preserved. We thus restrict our analysis to the first 28 states (the 28th state is the central state and indicated by an gray arrow in figure S1) and symmetrize the result to expand over the higher-frequency states. Theoretically the eigenvectors of the tight-binding Hamiltonian are normalized in both direction ($\sum_i |c_i^j|^2 = \sum_j |c_i^j|^2 = 1$), the experimentally extracted LDoS(i, j) should then also be normalized along both the frequency and position axis ($\sum_i \mathrm{LDoS}(i, j) = \sum_j \mathrm{LDoS}(i, j) = 1$). Since the antenna-coupling σ is slightly dependent on the frequency and the single resonance wavefunctions are overlapping [34], the sum of the raw resonance amplitudes over all positions (states) vary about 10 percent for different states (positions). We thus normalize the extracted wavefunction intensities in both dimensions by alternatingly normalizing them along one direction and then the other, until the difference in normalization along the both direction is of the order of 10^{-6}. We then consider that the extracted LDoS(i, j) is properly normalized along the two dimensions, which is especially important for the calculation of the fractal dimensions.

For the case, where the weak coupling is dominant, we measure, analyse and average over all 8 possible permutations. For the case, where the strong coupling is dominant there are 21 possible permutations in total, but 10 of the 21 permutations are actually mirrored sequences of the others. Since they are experimentally equivalent, we measure only the 11 different permutations that are not mirrored sequences of each other, but average over all 21 permutations by inverting the position axis for the mirrored ones.

Averaging each frequency-band of circular chains

The circular chains are made up of smaller motifs (i.e. $F_n = 3, 5, 8, 13, 21$), that we repeat N_p times, while imposing a weak coupling between two consecutive repetitions. The number of iteration N_p is chosen such that a ring of around 100 resonators is build for each F_n-motif. In this way, the F_n frequency bands expected for an infinite chain C_n are each populated with N_p states, and can be individually identified in each reflection spectrum $S_{11}(i, \nu)$ measured over each resonator i. In figure S2 one can see a photo of the circular chain of resonators for a motif length of $F_n = 13$, that was repeated 8 times. Com-

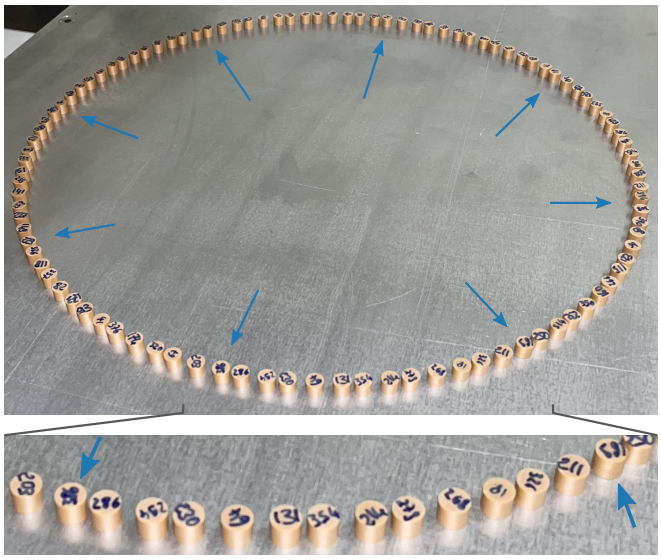

FIG. S2. (top) Photo of one circular chain, where the basic motif with length $F_n = 13$ is repeated $N_p = 8$ times, resulting in a total of 104 resonators. To emphasize the periodicity the first resonator of each repeated motif is marked with a blue arrow. (bottom) Zoomed in photo of one motif, where one can identify the "molecules" (dimers) and "atoms" (single resonator) that make up the chain.

pared to the linear chains where the lowest overlap was sought after to identify each state individually, for the circular chains we really want to create F_n energy bands as dense as possible. We therefore enhanced the stronger coupling to $t_B = 148\,\mathrm{MHz}$ and reduced the weaker coupling to $t_A = 55\,\mathrm{MHz}$, in order to obtain better isolated bands. Experimentally this was done by increasing the longer distance d_A to 9 mm (we keep the shorter distance at 7 mm) and by reducing the distance between the two metallic plates that sandwich the resonators from $\approx 12\,\mathrm{mm}$ to 8 mm. This alters the evanescent decay of the electromagnetic fields outside of the resonators.

Rearranging the sum over the different states, one can re-write

$$\rho(\vec{r_i}, \nu) = \sum_{j=1}^{F_n} \sum_{p=1}^{N_p} f_{\nu_{j,p},\Gamma_{j,p}}(\nu) \cdot |\psi_{j,p}(i)|^2 \,, \tag{S4}$$

where $\nu_{j,p}$ and $\Gamma_{j,p}$ are the resonance-frequency and -width of the p-th state within the j-th frequency band and $|\psi_{j,p}(i)|^2$ the corresponding wavefunction intensity measured over resonator i.

Supposing that the bands are sufficiently isolated, by integrating each frequency band j individually, one can then find

$$\mathrm{LDoS}(i,j) \propto \int_{\text{band } j} [1 - \Re S_{11}(i,\nu)] \, \mathrm{d}\nu \,, \tag{S5}$$

where we can further average over all indices i that have the same conumbering $c(i)$.

In figure S3 (left column) one can see the measured density of states $\mathrm{DoS}(\nu) = \langle 1 - \Re S(i,\nu) \rangle_i$ for all $F_n = 3, 5, 8, 13, 21$. Determining the integration borders of each band j is obvious for $F_n = 3$ and 5, where the F_n frequency bands are isolated and well separated by clearly visible gaps. While for $F_n = 8$ one could eventually still identify 8 bands, although some gaps in between are closing, it becomes impossible for higher n to directly identify all frequency-bands. We therefore calculate the integrated density of states $\mathrm{iDoS}(\nu) = \int^{\nu} \mathrm{DoS}(\nu')\mathrm{d}\nu'$, that we normalize so that when integrating over all states the $\mathrm{iDoS}(\nu)$ equals F_n, the total number of bands ($\int \mathrm{DoS}(\nu')\mathrm{d}\nu' = F_n$). Theoretically in the limit of $\Gamma \to 0$ and perfectly normalized wave functions, we would obtain a staircase function where we would have F_n big steps with step-height 1, that are constituted of N_p smaller steps, with height $1/N_p$. Since the step corresponding to a single band has a height of 1, one could think of intersecting the $\mathrm{iDoS}(\nu)$ with a set of horizontal lines that have a spacing of 1 in between them. The found intersecting points ν_k^* ($\mathrm{iDoS}(\nu_k^*) = k$, for all $k \in (0, 1, 2, ..., F_n)$ could then define the integration intervals for each band.

Due to the non-zero linewidth of our resonances, the N_p smaller steps within a band are completely blurred, while only the plateaus corresponding to the well visible gaps, remain. Since the antenna-coupling σ is slightly dependent on the frequency, and the single resonance wavefunctions are slightly overlapping [34], the different states are not properly normalized in the experiment, which translates to slighlty different step-heights in the iDoS. So just intersecting the experimental iDoS with equally spaced lines, does not work very well, as can be seen for the case of $F_n = 3$, where the two clearly visible plateaus are not at $\mathrm{iDoS}(\nu) = 1$ and $\mathrm{iDoS}(\nu) = 2$, as expected if properly normalized, but slightly higher. We thus use a hybrid approach where we take the frequency-positions of the clearly visible gaps as fixed references and find the frequency-position of the vanished gaps in between by intersecting the iDoS in between with equally spaced lines. The position of the visible gaps are extracted by hand and marked as solid black vertical lines in the first two columns of figure S3. At the positions where the solid black lines intersect the iDoS we draw solid blue horizontal lines. For $F_n = 3, 5, 8$ we were able to identify all gaps, so the solid blue lines divide the iDoS in F_n intervals, but as explained earlier for $F_n = 13, 21$ not all gaps can be identified. Whenever we could not identify a gap, we draw additional blue dashed horizontal lines, that equally divide the space in between the two solid blue lines by the number of bands that we expected to be in between the clearly visible gaps. In order to not adjust our results by our expectations we estimate the number of bands in between two clearly visible gaps (solid blue lines), by rounding the position where the blue lines intersect the iDoS-axis to the nearest integer value

and suppose that this is the number of bands below that gap. That way we determine the number of bands in between two solid blue lines. At the frequencies where the dashed blue lines intersect the iDoS we draw dashed black vertical line. The black vertical (solid and dashed) lines then define the integration boundaries, that we use to integrate each individual spectrum measured over each resonator, leading to LDoS(i, j).

The results can be seen in figure S3, where LDoS(i, j) is plotted ordered according to the resonator position indexes i (third column) and to the conumber indexes $c(i)$ (forth column). By averaging LDoS$(c(i), j)$ over all sites that share the same conumber index, one obtains the smoothed patterns plotted on Figure 4. Unlike the procedure for linear chains, we do not need to symmetrize our results since this approach allows to analyse the whole frequency range. For the normalization, the procedure is the same.

Fractal Dimensions of the wavefunctions

We perform a multifractal analysis of the LDoS displayed in Fig. 2. The fractal dimension $D_q^{\psi}(j)$ for each state j is defined via an exponential scaling of the generalized inverse participation ratio $\chi^{(n)}(j)$ with the system size F_n (see (1)), and the spectrally averaged fractal Dimension $\overline{D_q^{\psi}}$ is defined by the scaling of the arithmetic average $\left\langle \chi^{(n)}(j) \right\rangle_j$ over all states in the spectrum. In order to investigate the scaling behaviour as a function of the system size one would have to perform the experiment for different system sizes F_n, which is impractical in our case, because the maximal possible system size in order to resolve all wavefunction is 55, which is far from the quasiperiodic limit. Fortunately there is another approach that is commonly used to calculate (fractal) dimensions in various fields of physics and mathematics, which is a box-counting algorithm. The method that we use and present in the following section has already proven itself in the characterization of chaotic system and multifractal wavefunctions at critical transisions and in quasiperiodic structures [3, 5, 16, 43].

Calculation via a Box-counting algorithm

The main idea behind the box-counting method is to break down the system into small "boxes" and analyse them individually. By changing the box size and considering smaller and smaller boxes, one can thus deduce scaling properties for the system. We use in the following the notations and formalism presented in reference [43]. We start by dividing our system of size F_n into $B = F_n/L$ boxes of size L. Since the system is one dimensional the boxes are actually intervals of length L. We then study the spatial distribution of each wavefunction $\psi_j(i)$ by calculating the probability

$$\mu_b(\psi_j, L) = \sum_{i \in \text{box } b} |\psi_j(i)|^2 \tag{S6}$$

to find a "ball" inside box b. Repeating this procedure for different box-sizes L, one can then compute the mass exponent

$$\tau_q = \lim_{L \to 0} \frac{\ln \langle P(q, \psi_j, L) \rangle_j}{\ln L/N} = \lim_{L \to 0} \frac{\ln \left\langle \sum_{b=1}^{B} \mu_b(\psi_j, L)^q \right\rangle_j}{\ln L/N} \tag{S7}$$

by linear fitting the spectrally averaged quantity $\ln \langle P(q, \psi_j, L) \rangle_j$ versus $\ln L$ and extracting the slope. For our system of size $F_n = 55$, we consider all box sizes $L = 1, 5, 11, 55$ with integer ration F_n/L. In Fig. S4 we plot and fit $\ln \langle P(q, \psi_j, L) \rangle_j$ versus the box-size $\ln L$ for some typical values of q. We find an excellent agreement between the data points and fit. From the mass exponents τ_q one can then easily obtain the spectrally averaged fractal dimension $D_q = \tau_q/(q-1)$.

Comparison to numerical results

In Fig. 3 one can see the calculated experimental fractal Dimension $\overline{D_q^{\psi}}$, the theoretical prediction as well as an confidence interval for our measurement. Both the positioning of the resonators as well as the resonance frequency of each resonator have a small variance, which leads to slightly different tight-binding Hamiltonians, wavefunctions and thus fractal dimensions each time one would perform the experiment.

The fluctuation of the resonance frequencies have two origins. To place the resonators, we let them drop through a small precision machined down-tube and then apply slight pressure via an plastic rod on top of the dielectric cylinders. This ensures a good electrical contact between the bottom plate and the resonator, but upon replacing the same resonator several times, the measured resonance frequencies of the very same resonator still vary slighly with a standard deviation of ≈ 0.5 MHz. Further, the resonators are not identical, resulting in different resonance frequencies as well. Out of a series of 500 resonators, whose resonance frequencies follow approximately a normal distribution with a width of 40 MHz, we chose the 55 resonators that have the closest resonance frequencies. This results in a difference between the extreme resonance frequencies of ≈ 3 MHz. Since the span of 3 MHz is small compared to the width of the distribution of resonance frequencies for the whole series, we suppose that they follow a quasi linear distribution. In addition, we have small variations within the positions upon placing the resonators, that result in slightly varying coupling strength's. In space, these fluctuations are

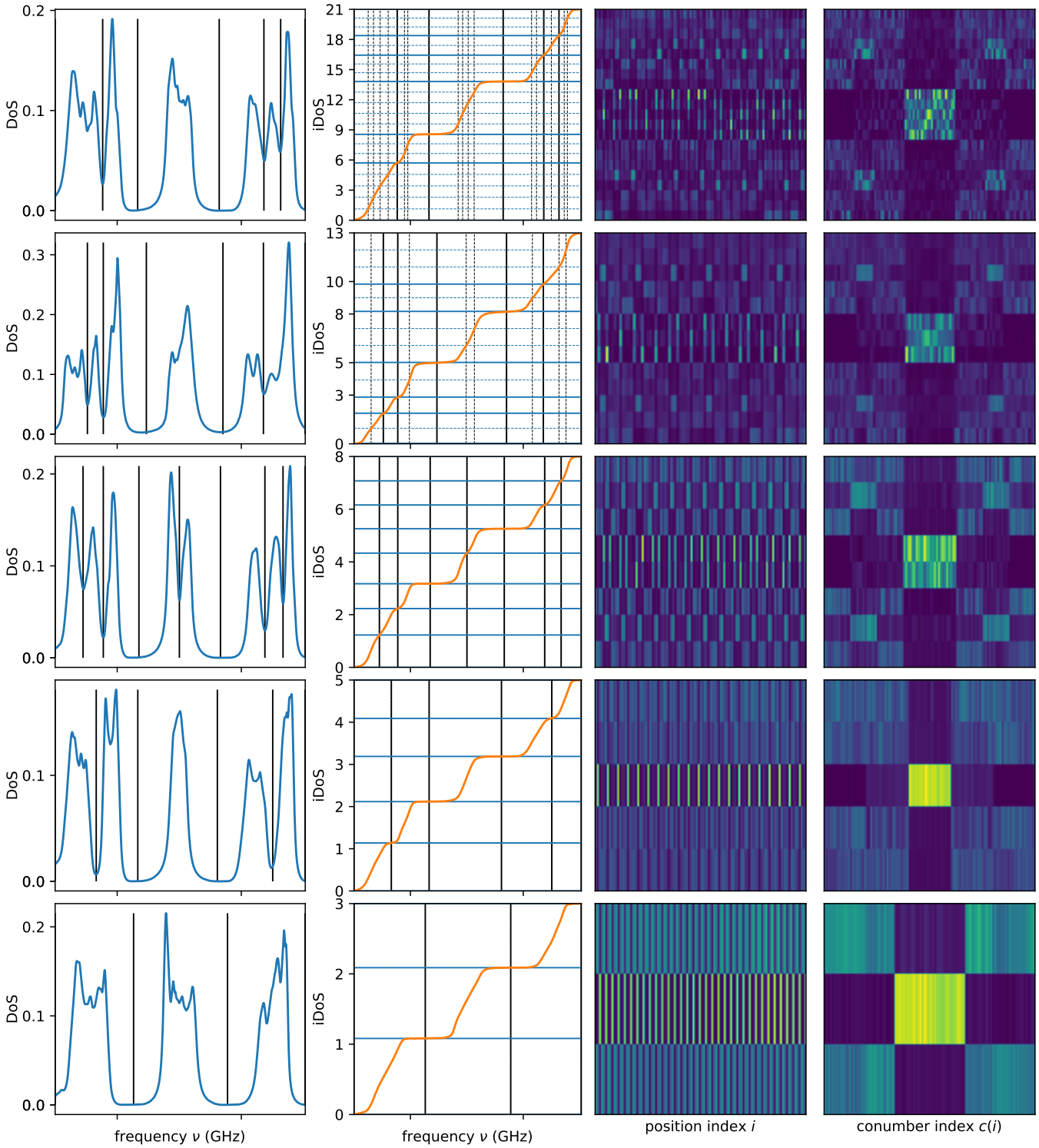

FIG. S3. From the top to the bottom: The different steps of the data treatment procedure for the circular chains with (first row) $F_n = 21$, (second row) $F_n = 13$, (third row) $F_n = 8$, (forth row) $F_n = 5$ and (fifth row) $F_n = 3$. For each chain we plot (from the left the right) (first column) the density of states DoS(ν) and (second column) the integrated density of states iDoS(ν) as a function of the frequency ν. The black and blue horizontal and vertical lines define the integration boundaries to extract LDoS(i, j), that are arranged according to the position index i (third column) and conumber index $c(i)$ (forth column). The vertical axis of the third and forth column corresponds to the frequency-index j.

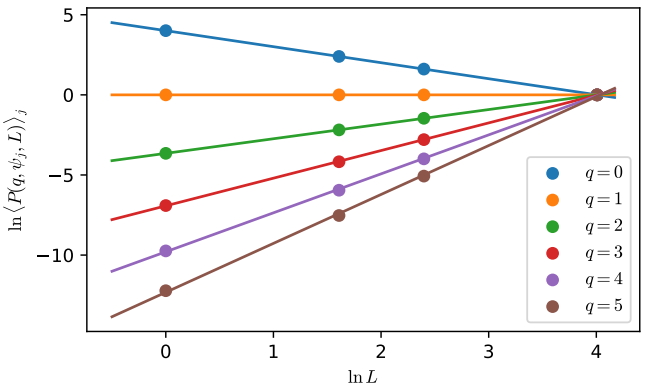

FIG. S4. Calculated $\ln\langle P(q,\psi_j,L)\rangle_j$ for the different box sizes L and some example values of q. For each q the data points are fitted individually (solid lines), in order to extract their slope.

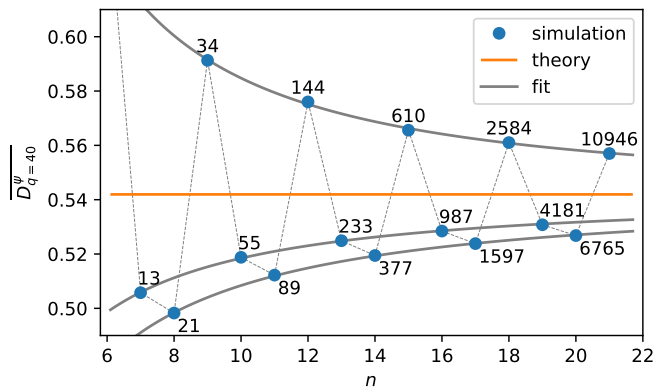

FIG. S5. Simulated spectrally averaged fractal dimension $\overline{D^{\psi}_{q=40}}$ for a high value of $q=40$ as a function of the iteration index n (blue points). The numbers near the blue points are the system size/motif length F_n for each iteration. The orange line presents the theoretical value of the fractal Dimension of the quasiperiodic system $\overline{D^{\text{theo}}_{q=40}}$. The grey solid lines are fits of the form $D(n) = An^B - y_0$.

of the order of 0.05 mm, that induces in the worst case (almost touching resonators) a variation of 4% of the coupling strength.

In order to estimate the impact of these experimental fluctuation on the extracted fractal dimensions, we simulate the experiment by formulating simple tight binding Hamitonians for the 11 different permutations. We model the resonators resonance frequencies $\nu^* \sim 7.454\,\text{MHz} + \mathcal{U}(-1.5\,\text{MHz}, 1.5\,\text{MHz}) + \mathcal{N}(0,\sigma_\nu)$ by employing a uniform distribution with a span of 3 MHz combined with a normal distribution with $\sigma_\nu = 0.5\,\text{MHz}$ centered around 7.454 GHz, that accounts for the variation upon re-placing the same resonator several times. With $\{\vec{r_i}\}$ being the exact positions that follow the Fibonacci sequence, we suppose that the actual positions of the resonators $\{\vec{r_i^*}\}$ follow $\vec{r_i^*} \sim \vec{r_i} + \mathcal{N}(0,\sigma_{\text{pos}})$, supposing a normal distribution with a standard deviation of $\sigma_{\text{pos}} = 0.5\,\text{mm}$ in the x and y direction. We then calculate the coupling strength between all nearest neighbours i and k, by calculating their distances $d_{ik} = |\vec{r_i^*} - \vec{r_k^*}|$ and using the relation $t(d) = 63.2\,\text{MHz}\cdot K_0(0.481\,\text{mm}^{-1}\cdot d/2)\cdot[K_2(0.481\,\text{mm}^{-1}\cdot d/2) + K_0(0.481\,\text{mm}^{-1}\cdot d/2)]$ between coupling strength t and separation d between two resonators that was extracted from two-resonator measurements [34]. We diagonalize the Hamitonians in order to find the wavefunctions, average over the different permutations and determine the fractal Dimensions D^*_q via the same box-counting method that we use for the experiment. We perform this procedure 10000 times and then for each q the 5-th percentile and 95-th percentile of the distribution of D^*_q are used as the lower and higher contour line of the grey area in Fig. 3 respectively, defining a sort of 90% confidence interval.

There is a noticeable offset for large values of q between the experimental $\overline{D^{\psi}_q}$ and the theory. The fact the values for one experimental realization have an offset could be explained by experimental fluctuation, since both the experimental points as well as the theoretical curve lie within the confidence interval, but the average values of the simulated D^*_q (white dashed line within the grey area in Fig. 3) shows an offset compared to the theoretical curve as well. Next-neighbour couplings within the actual experiment and the way we average over the 11 permutations play certainly a small role, but this offset mainly arises form the finite system size of $F_n = 55$.

In Fig. S5 one can see calculated fractal dimensions $\overline{D^{\psi}_{q=40}}$ for different system sizes F_n for a high value of $q = 40$ and $\rho = 0.64$. Since here we only want to compare the effect of the system size, we simulate the only-nearest neighbour tight-binding system of the n-th periodic approximate of infinite size by formulating a closed chain of F_n resonators (one single motif) and F_n couplings where we vary over the phase of the connecting coupling between the first and last resonator to account for the periodicity. One can see that the fractal dimensions converge to the theoretical value in the quasi periodic limit $n \gg 1$, with an oscillating behaviour. A quick explanation of this feature can be given, when looking into the central/most localized state. If the system size is an uneven number the central state is localized only at the central site, while for an even system size, the central state is localized at the two central positions of $c(i)$. It is thus less localized and therefore it has a greater fractal dimension. Since numerically it is very costly to diagonalize very large matrices, we stop our-self at a system size of $F_{21} = 10946$, which still has an noticeable offset compared to the theoretical value. Then in order to verify that the values converges to the theoretical value, we fit the apparent three different subsets with

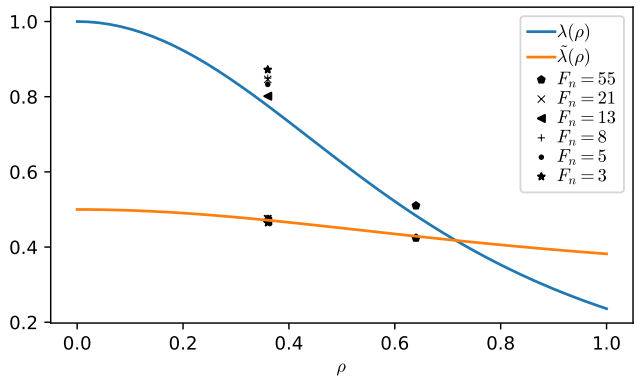

FIG. S6. The theoretical renormalization factors λ (blue line) and $\tilde{\lambda}$ (orange line) as a function of ρ. The experimentally extracted renormalization factors for the different motif lengths F_n are plotted at their corresponding ρ with different black symbols.

an algebraic decay $D(n) = An^B - y_0$, where we suppose the same exponent B and offset y_0 for all subsets but with different amplitudes A. We find $B = -1.298$ and $y_0 = 0.540$, which corresponds reasonable well to the theoretical value $\overline{D^{\text{theo}}_{q=40}} = 0.542$, considering that the theory was formulated in the strong modulation regime $\rho \ll 1$, where we are far off with $\rho = 0.64$.

Renormalization factors $\lambda(\rho)$ and $\tilde{\lambda}(\rho)$

Within the renormalization theory (for the weak coupling dominant case), on obtains a direct recursive construction law for the LDoS (see eq. (3) and (4)), where the two renormalization factors

$$\tilde{\lambda}(\rho) = \frac{2}{(1+\rho^2)^2 + \sqrt{(1+\rho^2)^4 + 4\rho^4}} \tag{S8}$$

and

$$\lambda(\rho) = \frac{1}{1 + \rho^2\gamma(\rho) + \sqrt{1 + (\rho^2\gamma(\rho))^2}} \tag{S9}$$

with $\gamma(\rho) = 1/1(1+\rho^2)$, are both dependent on the ratio of the coupling strength ρ [28].

In order to experimentally estimate the renormalization factors we make use of the fact that the sum over all states and positions of the LDoS for a system with motif length F_n, sums up to F_n because each of the F_n states were properly normalized ($\sum_i |\psi_j(i)|^2 = 1$).

We can thus sum up all the pixels that contribute to the central square of the LDoS (corresponding to atomic sites and states) and divide it by the side length of that square (i.e. the number of atomic sites within the chain) to find the renormalization factor $\tilde{\lambda}$ for the atomic sites/states. For the molecular sites/states we proceed in the same way, but additionally we average over the four corner squares (corresponding to molecular sites and states).

Since we chose to use different couplings for the linear chains and the circular chains, we experimentally can invest the renormalization factor for two different values of ρ: $\rho = 0.64$ for the linear chains of $F_n = 55$ resonators and $\rho = 0.37$ for the circular chains with smaller motif length. In Fig. S6 one can see the two theoretical curves for $\lambda(\rho)$ and $\tilde{\lambda}(\rho)$ as a function of ρ, that we compare to the experimentally extracted values (black symbols).

The experimentally extracted renormalization factors $\lambda(\rho)$ and $\tilde{\lambda}(\rho)$ correspond reasonably well with their theoretical prediction, though the extracted $\lambda(\rho)$ for the molecular sites vary for the different motif length F_n and generally show a slight offset. This can be explained by the small system sizes F_n, since the theoretical predictions were formulated in the quasi periodic limit.